

Probing α clustering in ^{12}C at CSR energies using the Jet AA Microscopic Transport Model

Subhash Singha*

Institute of Modern Physics Chinese Academy of Sciences, Lanzhou 730000, China

²*State Key Laboratory of Heavy Ion Science and Technology,*

Institute of Modern Physics Chinese Academy of Sciences, Lanzhou 730000, China

(Dated: February 10, 2026)

We investigate the sensitivity of low-energy nuclear collisions to intrinsic nuclear structure by studying the interplay between initial-state geometry and final-state observables in C+C and C+Pb collisions at $\sqrt{s_{\text{NN}}} = 2.36$ GeV, relevant for experiments at the Cooling Storage Ring (CSR) facility in Lanzhou and forthcoming experiments at the High Intensity heavy-ion Accelerator Facility (HIAF) in Huizhou. Calculations are performed within the Jet AA Microscopic Transport Model (JAM) using Woods-Saxon and triangular α -clustered configurations for the ^{12}C nucleus. The initial geometry is characterized in terms of transverse size, compactness, eccentricities, and their event-by-event fluctuations. We find that α clustering leads to a more compact participant configuration than the Woods-Saxon case, while transverse-size and eccentricity fluctuations show only weak sensitivity to clustering. At this beam energy, radial observables remain sensitive to geometric compactness, with the proton mean transverse momentum $\langle p_T \rangle$ enhanced for α -clustered configurations, whereas pions show little sensitivity. The anisotropic response is examined using flow harmonic coefficients. We find an enhancement of the mean flow magnitudes, $\langle v_n \rangle = \sqrt{\langle v_n^2 \rangle}$, for α -clustered configurations at large N_{part} , while the event-by-event fluctuation strength of individual harmonics remains small. Symmetric cumulants of the initial-state eccentricities show sensitivity to clustering, whereas the corresponding correlations among final-state flow harmonics do not exhibit a comparably strong separation. These results indicate that radial observables and correlation-based flow measurements provide complementary probes of α clustering in low-energy nuclear collisions.

PACS numbers:

I. INTRODUCTION

In recent years, a new direction in relativistic heavy-ion physics has emerged that exploits the geometric and structural properties of the colliding nuclei as tools to probe both nuclear structure and the collective response of the produced medium. Experimental measurements have demonstrated that intrinsic nuclear deformation can leave observable imprints on final-state momentum anisotropies. In particular, the STAR Collaboration has reported clear signatures of the quadrupole deformation of uranium nuclei in U+U collisions at RHIC energies [1, 2], while measurements in Xe+Xe collisions at the LHC [3–5] have revealed sensitivity to the prolate deformation of the xenon nucleus through deviations from expectations based on spherical nuclei.

These developments have motivated growing interest in using light nuclei with pronounced intrinsic structure as controlled probes of initial-state geometry in nuclear collisions. In this context, collisions involving nuclei such as ^{12}C and ^{16}O are particularly intriguing, as they are predicted to exhibit strong α -cluster correlations in their ground-state wave func-

tions [6–12]. The intrinsic structure of ^{12}C , and in particular the nature of its Hoyle state, has been the subject of extensive theoretical and experimental investigations. While *ab initio* calculations based on effective field theory have suggested that the Hoyle state may resemble a linear chain of three α clusters [13], more recent experimental measurements favor a predominantly triangular α -cluster configuration [14, 15], indicating that its underlying geometry remains an active subject of study.

Recent experimental results from O+O collisions at RHIC [16] and the LHC [17–21], together with complementary theoretical studies, suggest that small-system collisions may retain sensitivity to such subnucleonic or cluster-scale geometric features. These observations open the possibility of accessing clustering effects through final-state observables in relativistic nuclear collisions. Since α clustering is an intrinsic feature of the initial coordinate-space geometry of the nucleus, its experimental manifestation necessarily relies on the efficiency with which these spatial correlations are dynamically translated into measurable momentum-space signatures.

At ultra-relativistic collision energies, the connection between nuclear geometry and final-state observables is commonly interpreted within a hydrodynamic framework. In this picture, initial-state spatial anisotropies and density inhomogeneities are effi-

*Electronic address: subhash@impcas.ac.cn

ciently converted into momentum-space correlations through the collective expansion of a nearly equilibrated medium. The system's response is predominantly governed by pressure gradients and transport properties, enabling nuclear structure effects to be investigated in a controlled manner via their influence on initial eccentricities and density profiles.

At lower collision energies, however, the dynamical evolution of the system is qualitatively different. Baryon stopping, finite net-baryon density, mean-field potentials, and hadronic rescattering play a central role and can substantially modify the mapping between the initial geometry and final-state observables. Consequently, it is not *a priori* evident whether, or to what extent, nuclear structure effects such as α clustering survive the subsequent evolution and remain observable. Determining how initial geometric features are preserved in this regime therefore constitutes an important open question and is essential for assessing the sensitivity of low-energy heavy-ion collisions to nuclear structure.

Recent and forthcoming experimental programs provide new opportunities to explore these questions. Experiments involving C+C and C+Pb collisions at $\sqrt{s_{NN}} = 2.36$ GeV have recently commenced at the Cooling Storage Ring (CSR) facility in Lanzhou [22–29]. In addition, the upcoming High Intensity heavy-ion Accelerator Facility (HIAF) [30–33] in Huizhou will enable similar studies with a variety of collision systems, including O+O and U+U. Significant efforts are also underway at the LHC, where collisions of nuclei with non-spherical or exotic configurations, such as deformed Ne+Ne systems [19, 34], have been performed recently. Together, these programs open a new avenue for systematically investigating nuclear structure effects across a wide range of collision energies.

II. JAM FRAMEWORK

In this work, we employ the Jet AA Microscopic Transport Model (JAM), a hadronic transport framework developed for the simulation of relativistic nuclear collisions over a broad range of beam energies [35?–40]. In JAM, the initial positions of nucleons inside each nucleus are sampled according to a prescribed nuclear density distribution, after which the collision dynamics are modeled as a sequence of binary hadron–hadron interactions combined with mean-field effects. The model describes the full time evolution of the system, from the initial nuclear overlap through the dense interaction stage to the final hadronic freeze-out.

For the present study, JAM (version 2.58) [41] is used in its mean-field mode, which incorporates nuclear equation-of-state effects through a momentum-

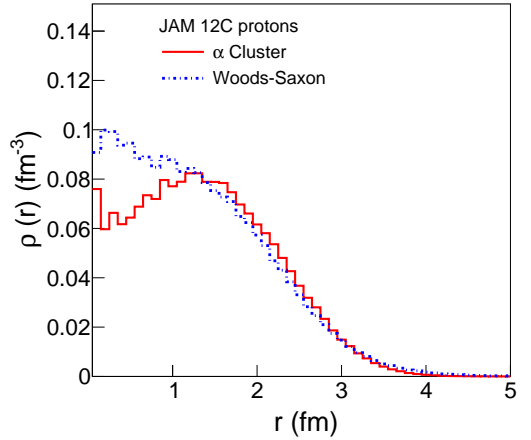


FIG. 1: Radial distribution of the point-proton density of ^{12}C obtained from JAM initial configurations for Woods-Saxon and α -clustered nuclei. The densities are normalized to the total proton number.

dependent potential that modifies the propagation of hadrons. This approach is essential at intermediate collision energies, where baryon stopping and mean-field interactions play a significant role in shaping collective dynamics. Events are generated for C+C and C+Pb collisions at $\sqrt{s_{NN}} = 2.36$ GeV, both with and without α clustering in the ^{12}C nucleus, where the implementation of clustering will be discussed in detail in the following section. We use the MD2 equation of state [39], characterized by a nuclear incompressibility of $K = 380$ MeV, which has been shown to successfully reproduce collective flow observables in low-energy heavy-ion collisions at RHIC and lower energies. The time evolution is followed up to 100 fm/ c with a time step of 1 fm/ c .

A. Clustering implementation

To investigate the role of nuclear structure effects, two distinct initial configurations are employed for the ^{12}C nucleus. In the reference configuration, nucleon positions are sampled from a spherical Woods-Saxon distribution. In the alternative configuration, ^{12}C is modeled as an α -clustered system consisting of three α clusters arranged at the vertices of an equilateral triangle in the transverse plane. This triangular configuration is motivated by nuclear structure studies, which have long predicted a pronounced three- α cluster structure in the ground state of ^{12}C [42–46]. Both transport and hydrodynamic models have been extensively employed to explore possible experimental signatures of nuclear

clustering in heavy-ion collisions over a wide range of beam energies [6–12].

The centers of the α clusters are separated by a fixed distance $d_{\alpha\alpha}$, which sets the characteristic length scale of the clustered geometry. Within each α cluster, the four constituent nucleons are distributed around the corresponding cluster center according to a Gaussian profile, $\rho_{\alpha}(\mathbf{r}) \propto \exp(-\mathbf{r}^2/2\sigma^2)$, where the width parameter σ controls the spatial localization of nucleons inside the cluster. In the present implementation, the values of $d_{\alpha\alpha}$ and σ are fixed for all events, while the overall orientation of the triangular configuration is randomized on an event-by-event basis. To prevent unphysical overlap between nucleons, a hard-core distance is imposed between all nucleon pairs.

The parameters of the α -clustered configuration ($d_{\alpha\alpha}=3.1$ fm and $\sigma=0.8$) are chosen such that the resulting point-proton density distribution and root-mean-square radius of ^{12}C remain comparable to those obtained from the Woods–Saxon configuration. This ensures that the two initial conditions differ primarily in their internal spatial organization and short-range correlations, rather than in their global size or average density, thereby enabling a controlled study of clustering-induced geometric effects. With this setup, JAM provides a consistent framework in which the impact of α clustering on the initial geometry and its subsequent influence on final-state observables can be systematically investigated while keeping the underlying transport dynamics and equation of state fixed.

The proton density distribution of ^{12}C is constructed from the initial-state nucleon configurations generated in JAM by accumulating proton coordinates over all events to obtain a spherically averaged density,

$$\rho_p(r) = \frac{1}{4\pi r^2} \frac{dN_p}{dr}, \quad (1)$$

which is normalized according to

$$\int d^3r \rho_p(r) = 6. \quad (2)$$

No additional smearing associated with the finite proton charge radius is applied, such that the resulting distribution corresponds to the point-proton density. The same procedure is used consistently for both Woods–Saxon and α -clustered initial configurations.

Differences between the two configurations arise primarily from their internal spatial structure rather than from the global density scale. In particular, α clustering modifies short-range correlations and local proton packing while leaving the angle-averaged density largely unchanged. This is reflected in the fact that the root-mean-square (RMS) radius of the

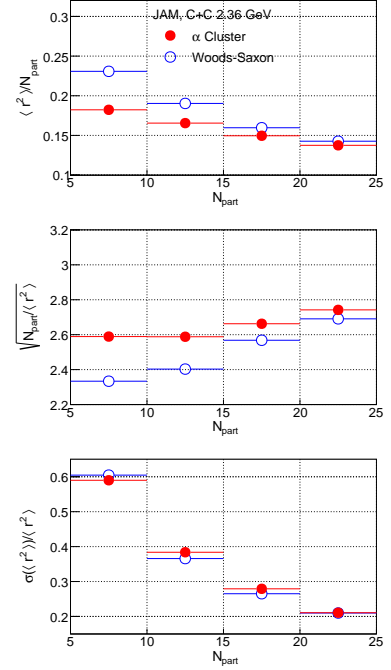


FIG. 2: The transverse size ($\langle r^2 \rangle$), compactness (C) and event-by-event transverse-size fluctuations as a function of N_{part} for Woods–Saxon and triangular α -clustered initial configurations for C+C collisions at $\sqrt{s_{\text{NN}}} = 2.36$ GeV.

Woods–Saxon configuration of ^{12}C is $r_{\text{rms}} \simeq 2.4$ fm, while that of the α -clustered configuration is $r_{\text{rms}} \simeq 2.3$ fm, corresponding to a difference of less than 4%. This demonstrates that the observed differences in initial-state compactness and in the final-state proton mean transverse momentum do not originate from trivial changes in the overall nuclear size or charge density, but instead reflect differences in the microscopic spatial organization of the nucleons.

III. RESULTS AND DISCUSSIONS

A. Correlation in initial-state geometries

To characterize the geometric properties of the initial participant configuration, we consider several complementary observables constructed from the transverse coordinates of participant nucleons. The average transverse size is quantified by the second moment

$$\langle r^2 \rangle = \frac{1}{N_{\text{part}}} \sum_{i=1}^{N_{\text{part}}} [(x_i - \bar{x})^2 + (y_i - \bar{y})^2], \quad (3)$$

where (\bar{x}, \bar{y}) denotes the transverse center of mass of the participants in a given event. To remove the

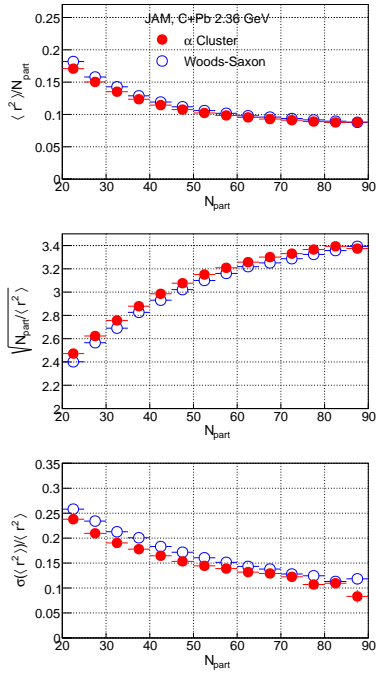


FIG. 3: The transverse size ($\langle r^2 \rangle$), compactness (C) and event-by-event transverse-size fluctuations as a function of N_{part} for Woods–Saxon and triangular α -clustered initial configurations for C+Pb collisions at $\sqrt{s_{\text{NN}}} = 2.36$ GeV

trivial scaling with the number of participants, we also study the scaled transverse size $\langle r^2 \rangle/N_{\text{part}}$. The corresponding compactness of the participant zone is defined as

$$C \equiv \sqrt{\frac{N_{\text{part}}}{\langle r^2 \rangle}}, \quad (4)$$

which provides a measure of the inverse transverse length scale governing the initial pressure gradients. Event-by-event transverse-size fluctuations are quantified by the relative width

$$\frac{\sigma(\langle r^2 \rangle)}{\langle r^2 \rangle}, \quad (5)$$

evaluated at fixed N_{part} .

Figure 2 and 3 present scaled transverse size ($\langle r^2 \rangle/N_{\text{part}}$), compactness (C) and event-by-event transverse-size fluctuations as a function of N_{part} for Woods–Saxon and triangular α -clustered initial configurations for C+C and C+Pb collisions at $\sqrt{s_{\text{NN}}} = 2.36$ GeV. In C+C collisions, the α -clustered configuration exhibits a systematically smaller scaled transverse size than the Woods–Saxon case, indicating a more compact spatial arrangement of the participant nucleons. This reduction

in $\langle r^2 \rangle/N_{\text{part}}$ is accompanied by a corresponding enhancement of the compactness over the full N_{part} range. In contrast, the relative transverse-size fluctuations show a weaker sensitivity to clustering, with comparable magnitudes for Woods–Saxon and α -clustered configurations. While the magnitude of fluctuations decreases with increase in N_{part} . The observed pattern demonstrates that, in symmetric light–light collisions, α clustering primarily shifts the average transverse scale of the system rather than significantly enhancing event-by-event size fluctuations.

A different behavior is observed in C+Pb collisions. While the average compactness remains larger for the α -clustered configuration, reflecting the increased local packing of nucleons in the carbon projectile, the relative transverse-size fluctuations are comparable or slightly larger for the Woods–Saxon case. In this asymmetric system, fluctuations of the transverse size are dominated by the geometry and participant fluctuations on the Pb side, which reduces the relative impact of clustering in the lighter nucleus. Consequently, α clustering continues to modify the mean transverse geometry but does not lead to an enhancement of transverse-size fluctuations. Overall, the comparison shown in Figures 2 and 3 demonstrates that α clustering predominantly affects the average compactness of the participant zone, while its influence on transverse-size fluctuations is comparatively modest and predominant at low N_{part} ranges.

In addition to transverse size observables, the anisotropic geometry of the initial participant configuration is usually characterized using event-by-event eccentricities ε_n . For each event, participant nucleons are identified and their transverse coordinates (x_i, y_i) are evaluated relative to the participant center of mass. The eccentricity coefficients are defined using weighted moments of the participant distribution [47],

$$\varepsilon_n = \frac{\sqrt{\langle (w_n \cos(n\phi))^2 + (w_n \sin(n\phi))^2 \rangle}}{\langle w_n \rangle}, \quad (6)$$

where $\phi = \tan^{-1}(y/x)$ is the azimuthal angle of a participant. For the dipole eccentricity ($n = 1$), the weight $w_1 = r^3$ is used, while for the elliptic ($n = 2$) and triangular ($n = 3$) eccentricities the weight $w_{2,3} = r^2$ is employed. These definitions follow standard prescriptions in studies of initial-state geometry and ensure sensitivity to long-wavelength shape deformations.

Event-averaged eccentricities are obtained as functions of N_{part} by averaging ε_n over events within a given N_{part} bin. Event-by-event fluctuations are quantified using the variance

$$\sigma(\varepsilon_n) = \sqrt{\langle \varepsilon_n^2 \rangle - \langle \varepsilon_n \rangle^2}, \quad (7)$$

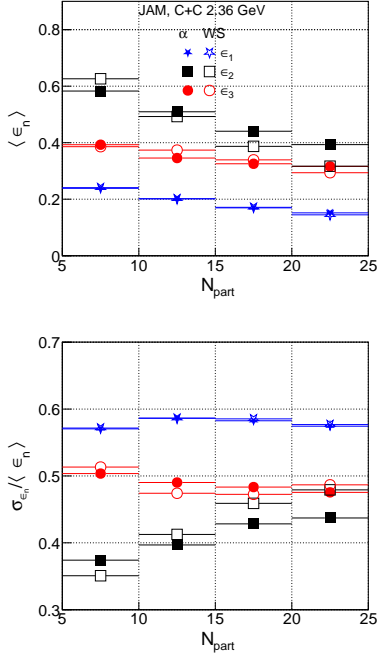


FIG. 4: Event averaged participant eccentricities and their event-by-event fluctuations as a function of N_{part} for Woods-Saxon and triangular α -clustered initial configurations for C+C collisions at $\sqrt{s_{\text{NN}}} = 2.36$ GeV.

as well as the corresponding relative fluctuation $\sigma(\varepsilon_n)/\langle \varepsilon_n \rangle$. These quantities characterize the intrinsic geometric variability of the initial state at fixed system size.

Figure 4 presents the average eccentricities ε_n and their event-by-event fluctuations as a function of N_{part} for C+C collisions. For both the Woods-Saxon and α -clustered configurations, the eccentricities follow the ordering $\varepsilon_2 > \varepsilon_3 > \varepsilon_1$, with comparable magnitudes in the two cases. The relative fluctuations of each ε_n remain approximately constant as a function of N_{part} , with the ordering $\sigma(\varepsilon_1) > \sigma(\varepsilon_3) > \sigma(\varepsilon_2)$.

For C+Pb collisions, the eccentricities are calculated in two distinct ways. First, to isolate the effect of the carbon projectile, we compute ε_n using only participants from the ^{12}C nucleus; these results are shown in Fig. 5. In the α -clustering case, ε_2 and ε_3 exhibit slightly opposite trends with N_{part} : one increases while the other decreases, and a crossing near $N_{\text{part}} \sim 60$. In contrast, for the Woods-Saxon configuration both ε_2 and ε_3 decrease with N_{part} . A similar pattern is observed in the relative fluctuations of ε_n .

Second, we compute the eccentricities using participants from both the Pb and C nuclei, which is the more natural choice for the full collision sys-

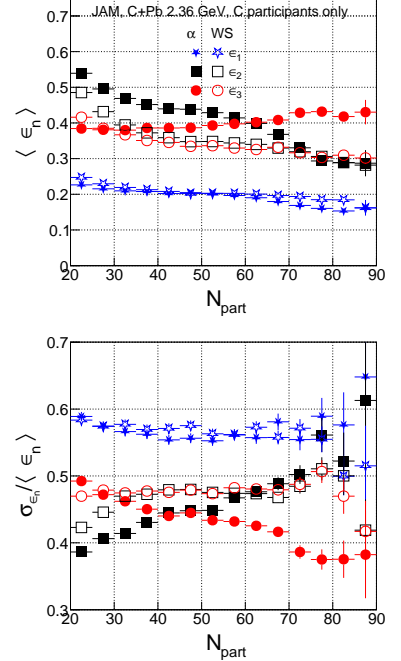


FIG. 5: Event averaged participant eccentricities and their event-by-event fluctuations as a function of N_{part} for Woods-Saxon and triangular α -clustered initial configurations for C+Pb collisions at $\sqrt{s_{\text{NN}}} = 2.36$ GeV. Results are calculated using C participants only (see text for details)

tem. These results are presented in Fig. 6. It is important to note that in both Figs. 5 and 6, the horizontal axis represents the total N_{part} from both nuclei. Although the C-only participant calculation showed clear differences between Woods-Saxon and α -clustering configurations, these differences become less obvious when participants from both target and projectile are included.

Correlations between different harmonic components of the initial geometry are further investigated using mixed moments such as $\langle \varepsilon_1 \varepsilon_3 \rangle$ and $\langle \varepsilon_2 \varepsilon_3 \rangle$, as well as their squared counterparts. These observables probe the degree to which different geometric deformations are correlated on an event-by-event basis and provide information beyond that contained in individual eccentricity magnitudes.

To quantify such correlations in a more systematic manner, we evaluate symmetric cumulants constructed from the eccentricities. For two harmonics m and n , the symmetric cumulant is defined as

$$\text{SC}\{m, n\} = \langle \varepsilon_m^2 \varepsilon_n^2 \rangle - \langle \varepsilon_m^2 \rangle \langle \varepsilon_n^2 \rangle, \quad (8)$$

where the angular brackets denote event averages at fixed N_{part} . Positive values of $\text{SC}\{m, n\}$ indicate a positive correlation between ε_m^2 and ε_n^2 , while neg-

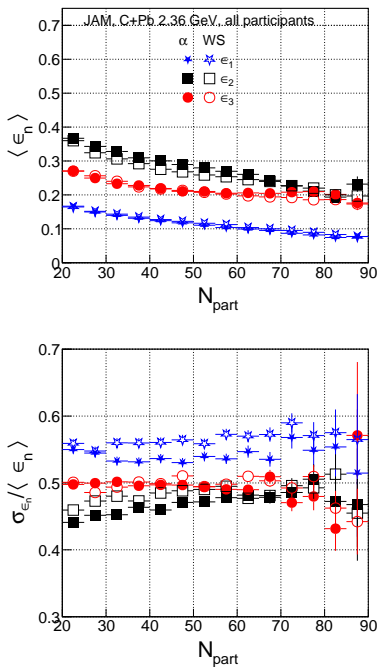


FIG. 6: Event averaged participant eccentricities and their event-by-event fluctuations as a function of N_{part} for Woods-Saxon and triangular α -clustered initial configurations for C+Pb collisions at $\sqrt{s_{\text{NN}}} = 2.36$ GeV.

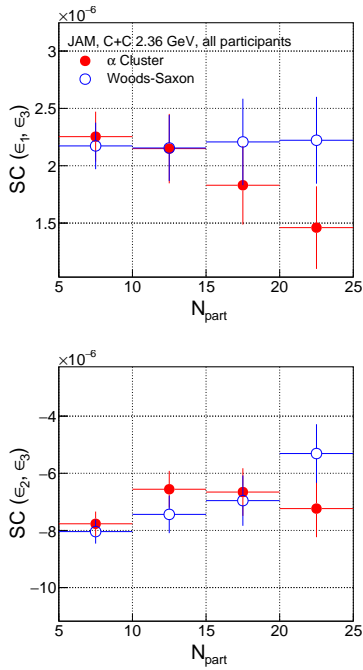


FIG. 7: Symmetric cumulants of eccentricities as a function of N_{part} for Woods-Saxon and triangular α -clustered initial configurations for C+C collisions at $\sqrt{s_{\text{NN}}} = 2.36$ GeV

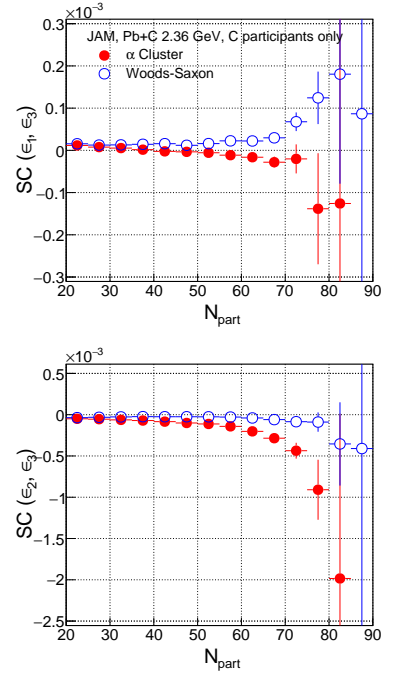


FIG. 8: Symmetric cumulants of eccentricities as a function of N_{part} for Woods-Saxon and triangular α -clustered initial configurations for C+Pb collisions at $\sqrt{s_{\text{NN}}} = 2.36$ GeV. Results are calculated using C participants only (see text for details)

ative values signal an anticorrelation. In this work, symmetric cumulants are evaluated for the harmonic combinations $(m, n) = (1, 3)$ and $(2, 3)$ as functions of N_{part} . For presentation purposes, the cumulants are scaled by N_{part} to reduce the trivial dilution of correlations with increasing system size.

The correlations among the eccentricities $\text{SC}\{\epsilon_1, \epsilon_3\}$ and $\text{SC}\{\epsilon_2, \epsilon_3\}$ are presented in Figs. 7, 8, and 9 for C+C collisions, C+Pb collisions with C participants only, and C+Pb collisions with all participants, respectively. In C+C collisions, no obvious differences are observed between the α -clustered and Woods-Saxon configurations. For C+Pb collisions when considering C participants only, $\text{SC}\{\epsilon_1, \epsilon_3\}$ in the Woods-Saxon case exhibits a positive correlation that increases with N_{part} , whereas the α -clustered case shows an opposite trend. For $\text{SC}\{\epsilon_2, \epsilon_3\}$, the Woods-Saxon configuration remains nearly constant around zero as a function of N_{part} , while the clustered configuration displays an increasingly negative correlation with increasing N_{part} . Similarly, when all participants are included, $\text{SC}\{\epsilon_1, \epsilon_3\}$ shows a positive correlation for both Woods-Saxon and clustered configurations, although the magnitude in the clustered case is smaller than that in the Woods-Saxon case. For

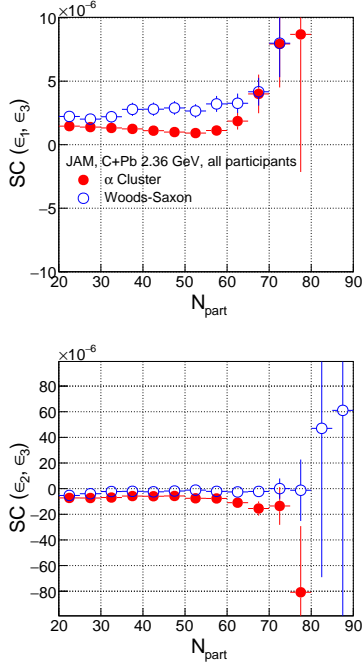


FIG. 9: Symmetric cumulants of eccentricities as a function of N_{part} for Woods–Saxon and triangular α -clustered initial configurations for C+Pb collisions at $\sqrt{s_{\text{NN}}} = 2.36$ GeV. Results are calculated using C participants only (see text for details)

$\text{SC}\{\varepsilon_2, \varepsilon_3\}$, the qualitative features are similar to those observed in the C-participants-only case, but with reduced magnitudes. These results indicate that α clustering can induce a negative correlation between ε_2 and ε_3 , which may be reflected in the final-state flow coefficients v_2 and v_3 , whereas the correlation between v_1 and v_3 may not be easily distinguishable between the two configurations.

B. Bulk observables with final-state particles

All observables defined in previous section are constructed solely from the initial-state nucleon positions and thus directly reflect the geometric properties of the participant configuration. The impact of these initial-state features on the collision dynamics is subsequently assessed through final-state observables, including the yield, mean transverse momentum of identified particles, flow coefficients v_n , and correlations between v_n and symmetric cumulants. This combined analysis allows for a systematic investigation of how initial-state geometry and clustering effects are transmitted to experimentally accessible final-state observables.

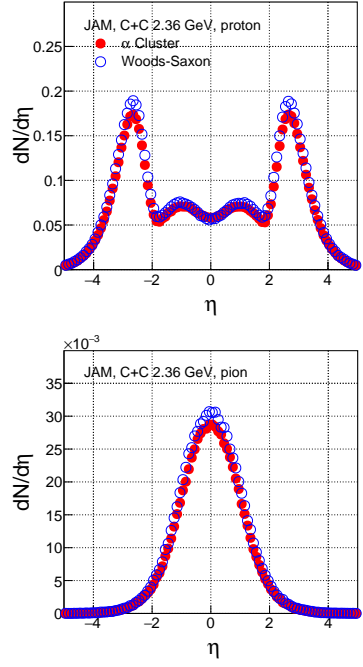


FIG. 10: $dN/d\eta$ of protons and pions for Woods–Saxon and triangular α -clustered initial configurations for C+C collisions at $\sqrt{s_{\text{NN}}} = 2.36$ GeV.

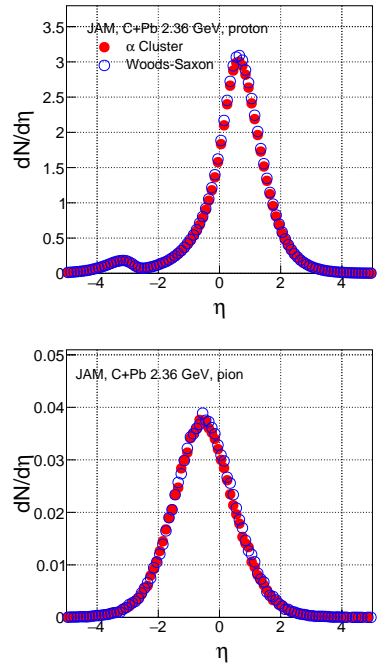


FIG. 11: $dN/d\eta$ of protons and pions for Woods–Saxon and triangular α -clustered initial configurations for C+Pb collisions at $\sqrt{s_{\text{NN}}} = 2.36$ GeV.

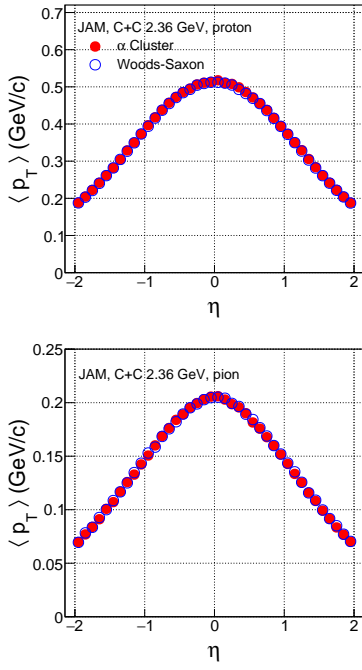


FIG. 12: $\langle p_T \rangle$ versus η of protons and pions for Woods-Saxon and triangular α -clustered initial configurations for C+C collisions at $\sqrt{s_{NN}} = 2.36$ GeV.

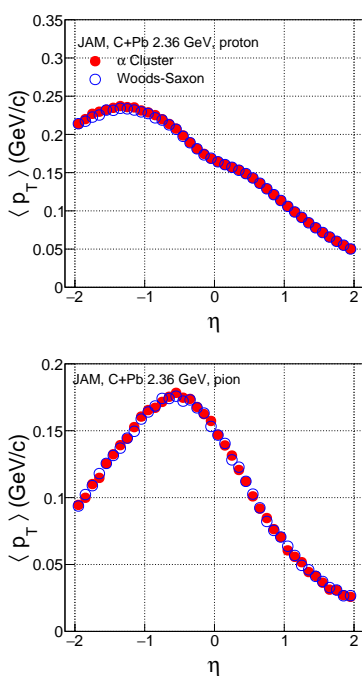


FIG. 13: $\langle p_T \rangle$ versus η of protons and pions for Woods-Saxon and triangular α -clustered initial configurations for C+Pb collisions at $\sqrt{s_{NN}} = 2.36$ GeV.

First, the bulk observables from produced particles are examined to assess the influence of α -clustering on final-state observables and their response to the initial-state geometry. Pseudorapidity distributions $dN/d\eta$ for protons and pions are shown in Fig. 10 for C+C collisions and in Fig. 11 for C+Pb collisions, with results presented for both Woods-Saxon and α -clustering configurations. The corresponding average transverse momentum $\langle p_T \rangle$ distributions are displayed in Fig. 12 and Fig. 13. In C+C collisions, $\langle p_T \rangle$ is symmetric about mid-rapidity, as expected for symmetric systems. In asymmetric C+Pb collisions, $\langle p_T \rangle$ distributions exhibit the expected asymmetry. When integrated over N_{part} , the bulk observables are found to be similar for both initial-state configurations.

C. Correlation in final-state particles

The observed hierarchy in participant-zone compactness and transverse-size fluctuations provides a natural geometric explanation for the stronger sensitivity of mean radial observables, such as the proton $\langle p_T \rangle$, to clustering effects compared to fluctuation-driven observables.

The event-wise mean transverse momentum of identified particles is defined as

$$\langle p_T \rangle_\alpha = \frac{1}{M_\alpha} \sum_{i=1}^{M_\alpha} p_{T,i}, \quad (9)$$

where α denotes the particle species and M_α is the corresponding multiplicity in a given event. Event-ensemble averages are obtained by further averaging $\langle p_T \rangle_\alpha$ over events at fixed N_{part} , which we denote by double angle brackets.

Event-by-event fluctuations of the mean transverse momentum are quantified using a two-particle correlator,

$$\delta p_{T,\alpha}^2 = \langle p_T p_T \rangle_\alpha - \langle p_T \rangle_\alpha^2, \quad (10)$$

where $\langle p_T p_T \rangle_\alpha$ is constructed from distinct particle pairs within the same event in order to remove self-correlations. This definition isolates dynamical fluctuations beyond trivial statistical contributions.

To probe relative changes between particle species, we also study the event-wise difference between the proton and pion mean transverse momenta,

$$\Delta p_T^{(p-\pi)} = \langle p_T \rangle_p - \langle p_T \rangle_\pi, \quad (11)$$

Figures 14 and 15 show $\langle p_T \rangle$ for protons and pions as a function of N_{part} in C+C and C+Pb collisions, respectively. In both collision systems, protons exhibit a larger $\langle p_T \rangle$ in the α -clustered configuration

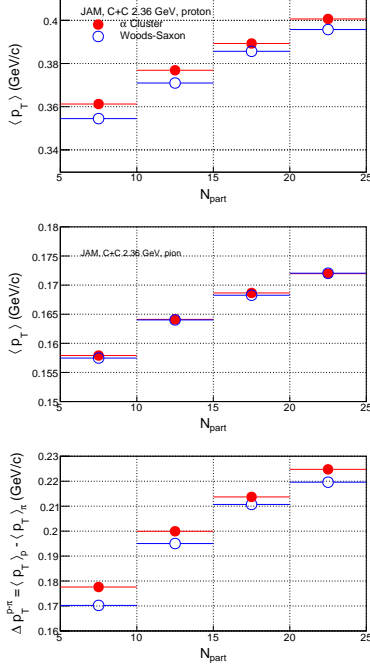


FIG. 14: $\langle p_T \rangle$ of protons and pions and their differences as a function of N_{part} for Woods–Saxon and triangular α -clustered initial configurations for C+C collisions at $\sqrt{s_{\text{NN}}} = 2.36$ GeV.

than in the Woods–Saxon case, whereas pions show no significant difference between the two configurations. This pattern is consistent with expectations based on the hierarchy of participant-zone compactness.

The difference in $\langle p_T \rangle$ between protons and pions is also shown. A clear distinction is observed in C+C collisions, while in C+Pb collisions the effect is most pronounced in the mid- N_{part} region.

To investigate the response to initial transverse-radius fluctuations, event-by-event dynamical transverse-momentum fluctuations are studied and quantified using a two-particle correlator,

$$\delta p_{T,p}^2 = \langle\langle \langle p_T p_T \rangle_p - \langle p_T \rangle_p^2 \rangle\rangle, \quad (12)$$

where $\langle p_T p_T \rangle_p = (Q_1^2 - Q_2)/[N(N-1)]$ is constructed from distinct particle pairs within the same event, with $Q_1 = \sum_i p_{T,i}$ and $Q_2 = \sum_i p_{T,i}^2$. This definition removes self-correlations and isolates dynamical fluctuations of the event-wise mean transverse momentum.

The results for C+C and C+Pb collisions are shown in Figs. 16 and 17, respectively. In both collision systems, the $\langle p_T \rangle$ fluctuations of protons are smaller in the α -clustered configuration than in the Woods–Saxon case, consistent with the reduced

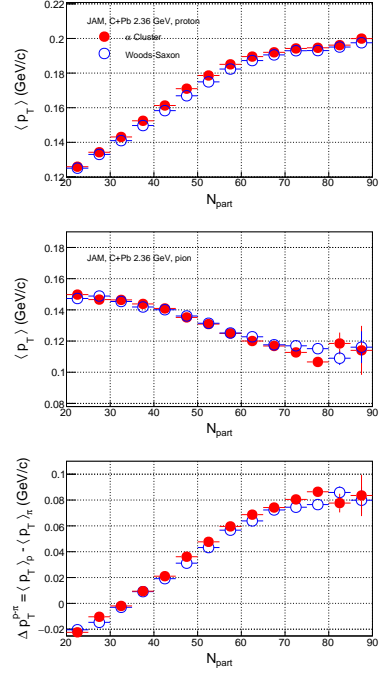


FIG. 15: $\langle p_T \rangle$ of protons and pions and their differences as a function of N_{part} for Woods–Saxon and triangular α -clustered initial configurations for C+Pb collisions at $\sqrt{s_{\text{NN}}} = 2.36$ GeV.

transverse-radius fluctuations of participant nucleons in the clustered configuration.

To characterize the magnitude and event-by-event fluctuations of the flow harmonics, we evaluate moments of the event-wise flow coefficients using the Q -vector formalism. For each event, the quantity $v_n^2 = |Q_n|^2/M^2$ is constructed, where $Q_n = \sum_i e^{in\phi_i}$ and M denotes the multiplicity of selected particles. The typical magnitude of the flow harmonics is characterized by $\langle v_n \rangle = \sqrt{\langle v_n^2 \rangle}$, while the fluctuation strength of a given harmonic is quantified by the variance $\langle v_n^4 \rangle - \langle v_n^2 \rangle^2$, with angle brackets denoting an average over events at fixed N_{part} .

Figures 18, 19, and 20 present the mean flow magnitude and its event-by-event fluctuations for the first-, second-, and third-order flow harmonics. Interestingly, we observe that α clustering leads to a significant enhancement of the mean flow magnitude, particularly at large N_{part} ($\gtrsim 70$). In contrast, the event-by-event fluctuation strength of individual harmonics remains small and is not clearly distinguishable within the current statistical precision. This indicates that α clustering primarily modifies the average initial geometry and its collective response, while inducing only modest changes in the magnitude of single-harmonic fluctuations. Consequently, precise experimental measurements of flow

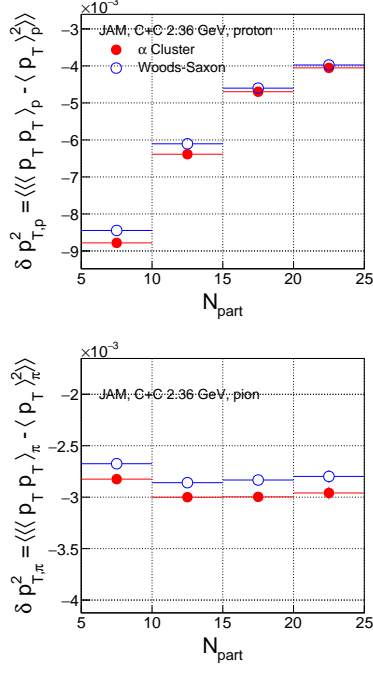


FIG. 16: Two particle $\langle p_T \rangle$ correlation of protons and pions as a function of N_{part} for Woods-Saxon and triangular α -clustered initial configurations for C+C collisions at $\sqrt{s_{\text{NN}}} = 2.36 \text{ GeV}$.

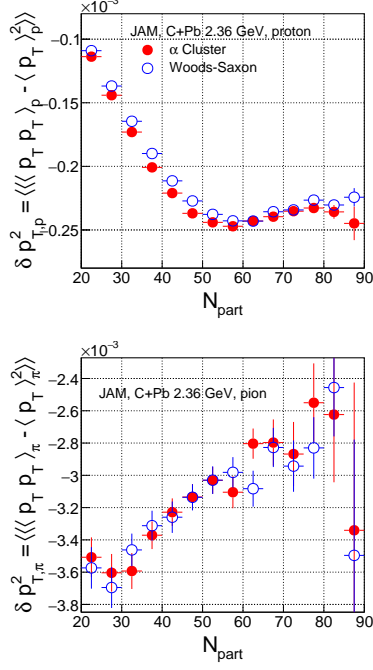


FIG. 17: Two particle $\langle p_T \rangle$ correlation of protons and pions as a function of N_{part} for Woods-Saxon and triangular α -clustered initial configurations for C+Pb collisions at $\sqrt{s_{\text{NN}}} = 2.36 \text{ GeV}$.

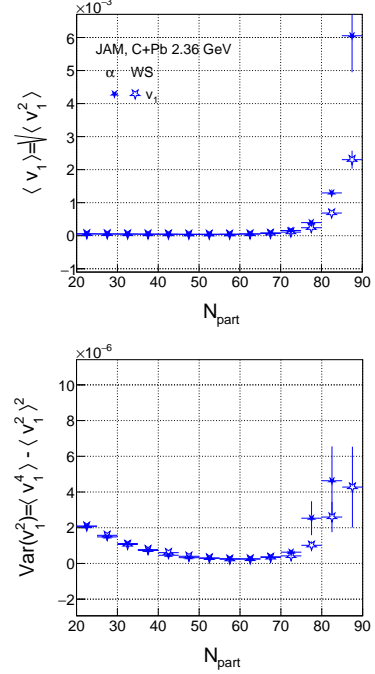


FIG. 18: $\langle v_1 \rangle$ and its event-by-event fluctuation as a function of N_{part} for Woods-Saxon and triangular α -clustered initial configurations for C+Pb collisions at $\sqrt{s_{\text{NN}}} = 2.36 \text{ GeV}$

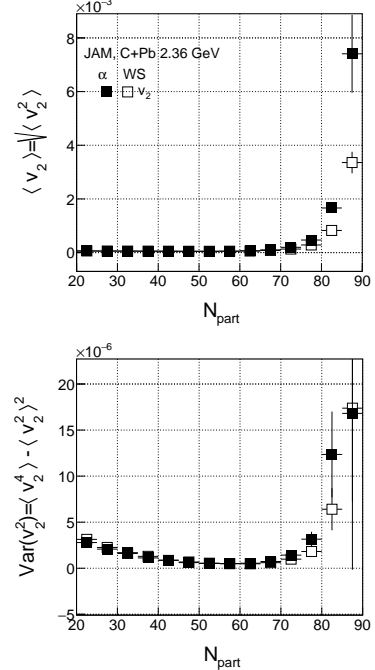


FIG. 19: $\langle v_2 \rangle$ and its event-by-event fluctuation as a function of N_{part} for Woods-Saxon and triangular α -clustered initial configurations for C+Pb collisions at $\sqrt{s_{\text{NN}}} = 2.36 \text{ GeV}$

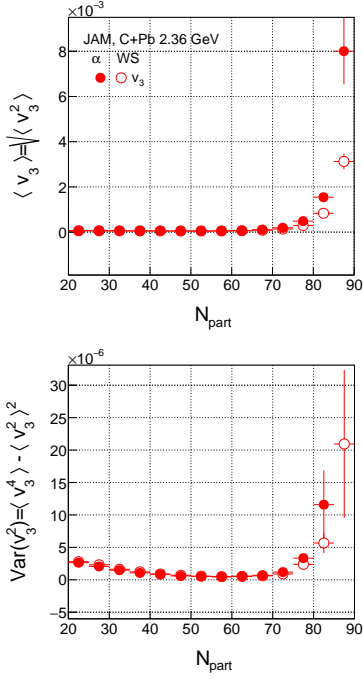


FIG. 20: $\langle v_3 \rangle$ and its event-by-event fluctuation as a function of N_{part} for Woods–Saxon and triangular α -clustered initial configurations for C+Pb collisions at $\sqrt{s_{\text{NN}}} = 2.36$ GeV

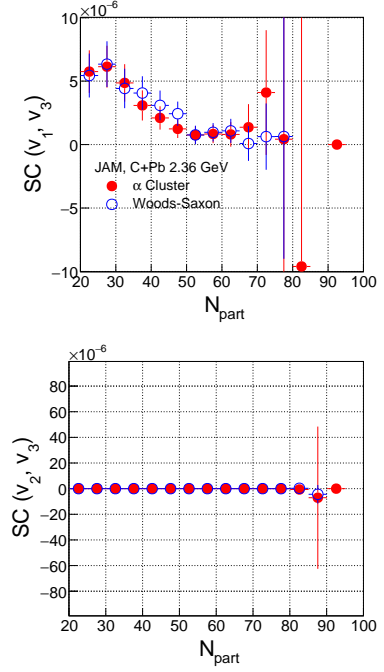


FIG. 21: Symmetric cumulants of v_n as a function of N_{part} for Woods–Saxon and triangular α -clustered initial configurations for C+Pb collisions at $\sqrt{s_{\text{NN}}} = 2.36$ GeV.

observables in this regime could provide valuable constraints on the presence and strength of α clustering in light nuclei.

Finally, symmetric cumulants of v_n are evaluated. Figure 21 shows $\text{SC}(v_1, v_3)$ and $\text{SC}(v_2, v_3)$ for C+Pb collisions. Both configurations yield a positive $\text{SC}\{v_1, v_3\}$, with no statistically significant distinction between them. The $\text{SC}(v_2, v_3)$ values are consistent with zero for both α -clustering and Woods–Saxon cases.

IV. CONCLUSION

In this work, we have investigated the sensitivity of low-energy nuclear collisions to intrinsic nuclear structure by studying C+C and C+Pb collisions at $\sqrt{s_{\text{NN}}} = 2.36$ GeV within the JAM transport model. By comparing Woods–Saxon and triangular α -clustered configurations for the ^{12}C nucleus, we systematically explored how initial-state geometric features propagate to final-state observables in a regime dominated by baryon stopping, mean-field interactions, and hadronic rescattering.

We find that α clustering leads to a more compact participant configuration than the Woods–Saxon case, while global transverse size and eccentricity

fluctuations exhibit only a weak sensitivity to clustering. The root-mean-square radii of the two configurations differ by less than a few percent, indicating that the observed effects are not driven by trivial changes in nuclear size, but rather by differences in the microscopic spatial organization of nucleons. At this beam energy, radial observables remain directly sensitive to such geometric compactness. In particular, the proton mean transverse momentum is enhanced for α -clustered configurations, whereas pion observables show little response. The $\langle p_T \rangle$ fluctuations of protons tend to be smaller in the α -clustered configuration than in the Woods–Saxon case, consistent with reduced transverse-radius fluctuations of participant nucleons in the clustered configuration.

The collective anisotropic response of the system is examined through the flow coefficients. We find that α clustering is associated with an enhancement of the mean flow magnitudes, $\langle v_n \rangle = \sqrt{\langle v_n^2 \rangle}$, at large N_{part} , consistent with modifications of the average initial geometry and its collective response. In contrast, the event-by-event fluctuation strength of individual flow harmonics remains small and is not clearly distinguishable within the present statistical precision. While symmetric cumulants constructed from the initial-state eccentricities exhibit a noticeable sensitivity to clustering, the corresponding correlations among final-state flow harmonics

do not show a comparably clear separation between clustered and unclustered configurations, suggesting that information on initial-state fluctuations is only partially retained during the dynamical evolution.

Overall, our results demonstrate that low-energy nuclear collisions retain measurable sensitivity to α clustering through a combination of radial observables and correlation-based flow measurements. We note, however, that the α -clustered configuration employed in this work represents a simplified geometric implementation, and that more realistic descriptions incorporating state-of-the-art nuclear structure calculations from low-energy nuclear physics will be essential for quantitative constraints on clustering effects. These findings highlight the

complementary roles of different classes of observables in probing intrinsic nuclear structure and provide strong motivation for future experimental measurements at CSR and HIAF.

Acknowledgments

SS thanks colleagues at the Institute of Modern Physics for valuable discussions. SS also thanks Dr. Amareesh Jaiswal and Dr. Sandeep Chatterjee for useful discussions during the WHEPP 2025 conference. SS acknowledges support from the Chinese Academy of Sciences.

[1] M. I. Abdulhamid et al. (STAR), *Nature* **635**, 67 (2024), 2401.06625.

[2] *Rept. Prog. Phys.* **88**, 108601 (2025), 2506.17785.

[3] S. Acharya et al. (ALICE), *Phys. Lett. B* **784**, 82 (2018), 1805.01832.

[4] A. M. Sirunyan et al. (CMS), *Phys. Rev. C* **100**, 044902 (2019), 1901.07997.

[5] G. Aad et al. (ATLAS), *Phys. Rev. C* **101**, 024906 (2020), 1911.04812.

[6] W. Broniowski and E. Ruiz Arriola, *Phys. Rev. Lett.* **112**, 112501 (2014), 1312.0289.

[7] W. B. He, Y. G. Ma, X. G. Cao, X. Z. Cai, and G. Q. Zhang, *Phys. Rev. Lett.* **113**, 032506 (2014), 1407.5414.

[8] M. Rybczyński, M. Piotrowska, and W. Broniowski, *Phys. Rev. C* **97**, 034912 (2018), 1711.00438.

[9] S. Zhang, Y. G. Ma, J. H. Chen, W. B. He, and C. Zhong, *Phys. Rev. C* **95**, 064904 (2017), 1702.02507.

[10] C.-C. Guo, W.-B. He, and Y.-G. Ma, *Chin. Phys. Lett.* **34**, 092101 (2017), 1803.07978.

[11] S. Y. Yao, X. G. Deng, and Y. G. Ma, *Phys. Rev. C* **112**, 024605 (2025), 2508.12582.

[12] L. Ma, Y. G. Ma, and S. Zhang, *Phys. Rev. C* **102**, 014910 (2020), 2007.10063.

[13] E. Epelbaum, H. Krebs, D. Lee, and U.-G. Meissner, *Phys. Rev. Lett.* **106**, 192501 (2011), 1101.2547.

[14] D. J. Marin-Lambarri, R. Bijkar, M. Freer, M. Gai, T. Kokalova, D. J. Parker, and C. Wheldon, *Phys. Rev. Lett.* **113**, 012502 (2014), 1405.7445.

[15] S. Shen, S. Elhatisari, T. A. Lähde, D. Lee, B.-N. Lu, and U.-G. Meißner, *Nature Commun.* **14**, 2777 (2023), 2202.13596.

[16] (2025), 2510.19645.

[17] A. Collaboration et al. (ALICE), *Phys. Lett. B* **869**, 139855 (2025), 2409.04343.

[18] S. Acharya et al. (ALICE), *Eur. Phys. J. C* **85**, 776 (2025), 2411.09334.

[19] G. Aad et al. (ATLAS) (2025), 2509.05171.

[20] G. Aad et al. (ATLAS), *Phys. Rev. Lett.* **136**, 032301 (2026), 2503.24125.

[21] A. Hayrapetyan et al. (CMS) (2025), 2510.02580.

[22] L. Lü, H. Yi, Z. Xiao, M. Shao, S. Zhang, G. Xiao, and N. Xu, *Sci. China Phys. Mech. Astron.* **60**, 012021 (2017).

[23] J. W. Xia et al., *Nucl. Instrum. Meth. A* **488**, 11 (2002).

[24] L. J. Mao et al., *JINST* **15**, T12015 (2020).

[25] S. H. Zhu, H. B. Yang, H. Pei, C. X. Zhao, X. Q. Li, and G. M. Huang, *JINST* **16**, P08014 (2021).

[26] L.-K. Liu, H. Pei, Y.-P. Wang, Y. Wang, B. Zhang, N. Xu, S.-S. Shi, and S. Shi, *Nucl. Sci. Tech.* **34**, 100 (2023), 2302.11759.

[27] A. K. Sahoo, X. He, Y. Nara, and S. Singha, *Phys. Rev. C* **109**, 054902 (2024), 2311.00946.

[28] D. Hu, X. Wang, M. Shao, Y. Zhou, S. Ye, L. Zhao, Y. Sun, J. Lu, and H. Xu, *Nucl. Instrum. Meth. A* **1057**, 168773 (2023), 2304.02944.

[29] W. Wu, X. He, Y. Ren, D. Shen, S. Shi, and X. Sun, *Nucl. Sci. Tech.* **37**, 60 (2026), 2503.22774.

[30] J. C. Yang et al., *Nucl. Instrum. Meth. B* **317**, 263 (2013).

[31] X. Zhou and J. Yang (HIAF project Team), *AAPPS Bull.* **32**, 35 (2022).

[32] J. Yang, *JACoW HIAT2025*, MOY01 (2025).

[33] *High Intensity heavy-ion Accelerator Facility*, <https://english.imp.cas.cn/hiaf/>, accessed: 2026-02-09.

[34] G. Giacalone et al., *Phys. Rev. Lett.* **135**, 012302 (2025), 2402.05995.

[35] Y. Nara, N. Otuka, A. Ohnishi, K. Niita, and S. Chiba, *Phys. Rev. C* **61**, 024901 (2000), nucl-th/9904059.

[36] T. Hirano, P. Huovinen, K. Murase, and Y. Nara, *Prog. Part. Nucl. Phys.* **70**, 108 (2013), 1204.5814.

[37] M. Isse, A. Ohnishi, N. Otuka, P. K. Sahu, and Y. Nara, *Phys. Rev. C* **72**, 064908 (2005), nucl-th/0502058.

[38] Y. Nara and H. Stoecker, *Phys. Rev. C* **100**, 054902 (2019), 1906.03537.

[39] Y. Nara, T. Maruyama, and H. Stoecker, *Phys. Rev. C* **102**, 024913 (2020), 2004.05550.

[40] Y. Nara and A. Ohnishi, *Phys. Rev. C* **105**, 014911 (2022), 2109.07594.

- [41] Y. Nara et al., *JAM: Jet AA Microscopic Transport Model*, <https://gitlab.com/transportmodel/jam2>, accessed: 2026-02-09.
- [42] L. R. Hafstad and E. Teller, *Physical Review* **54**, 681 (1938).
- [43] D. R. Harrington, *Phys. Rev.* **147**, 685 (1966).
- [44] K. Ikeda, N. Takigawa, and H. Horiuchi, *Progress of Theoretical Physics Supplement* **68**, 464 (1968).
- [45] J. V. Noble, *Phys. Lett. B* **31**, 253 (1970).
- [46] G. F. Bertsch and W. Bertozi, *Nucl. Phys. A* **165**, 199 (1971).
- [47] B. Alver and G. Roland, *Phys. Rev. C* **81**, 054905 (2010), [Erratum: *Phys. Rev. C* 82, 039903 (2010)], 1003.0194.